

Learning the Language of NVMe Streams for Ransomware Detection

Barak Bringoltz, Elisha Halperin, Ran Feraru, Evgeny Blaichman, Amit Berman
Samsung Semiconductor Israel Research and Development Center, Tel Aviv, Israel
{barak.b, elisha.h, ran.feraru, evgeny.bl, amit.berman}@samsung.com

Abstract

We apply language modeling techniques to detect ransomware activity in NVMe command sequences. We design and train two types of transformer-based models: the Command-Level Transformer (CLT) performs in-context token classification to determine whether individual commands are initiated by ransomware, and the Patch-Level Transformer (PLT) predicts the volume of data accessed by ransomware within a patch of commands. We present both model designs and the corresponding tokenization and embedding schemes and show that they improve over state-of-the-art tabular methods by up to 24% in missed-detection rate, 66% in data loss prevention, and 84% in identifying data accessed by ransomware.

1 Introduction

Ransomware is a cyber attack that encrypts a victim’s data until a ransom is paid. It is estimated that in 2021 the total global financial loss due to Ransomware was at the 20 billion USD scale, affecting healthcare, government, law enforcement, and education [1], and making it a serious threat to data privacy and to national security. Ransomware detection is an active area of research in cybersecurity with detection techniques belonging to one of two types: ‘static’ methods which identify malicious software signatures, and ‘behavioral’ methods, which detect patterns in the behavior of computing systems infected by ransomware. Especially, machine learning techniques are becoming widely used for detection, with features generated at different levels of the software stack – from low levels I/O to network activity [2].

Indeed, several works [3, 4, 5] use NVMe commands to detect ransomware by aggregating them into several dozens of statistical tabular features. In this work, we take a novel approach and especially:

1. We utilize the sequential nature of the NVMe command stream, and design our features and models to incorporate the time dimension of the data.
2. We work with raw NVMe command sequences, without aggregating them. In particular, we introduce an appropriate tokenization scheme, enabling the model to understand commands in their context. This allows us to output predictions for individual commands/patches of commands, and recognize ransomware patterns that would otherwise be lost to aggregation.
3. Finally, we show that our approach achieves superior results compared to SotA in key performance metrics such as missed detection rate and data loss prevention.

In Figure 1 we show a high-level view of our ransomware detection pipeline, and present two distinct approaches to model the problem. The first (Figure 1a) classifies individual commands into ransomware or benign, while the second (Figure 1b) works on patches of commands and predicts the fraction of ransomware they contain. As we will show, both approaches perform better than current SotA, yet each has its advantages compared to the other. The first detects ransomware faster, while the second detects more ransomware overall. Thus in the following sections, we present both, along with the way they process, tokenize, and model the NVMe stream, and the viability of their implementation in a product.

2 Data Processing

NVMe data is the set of sequential commands the Operating System (OS) sends the controller of a storage device, instructing it what data to read or write. An NVMe command comprises of four fundamental attributes: the floating

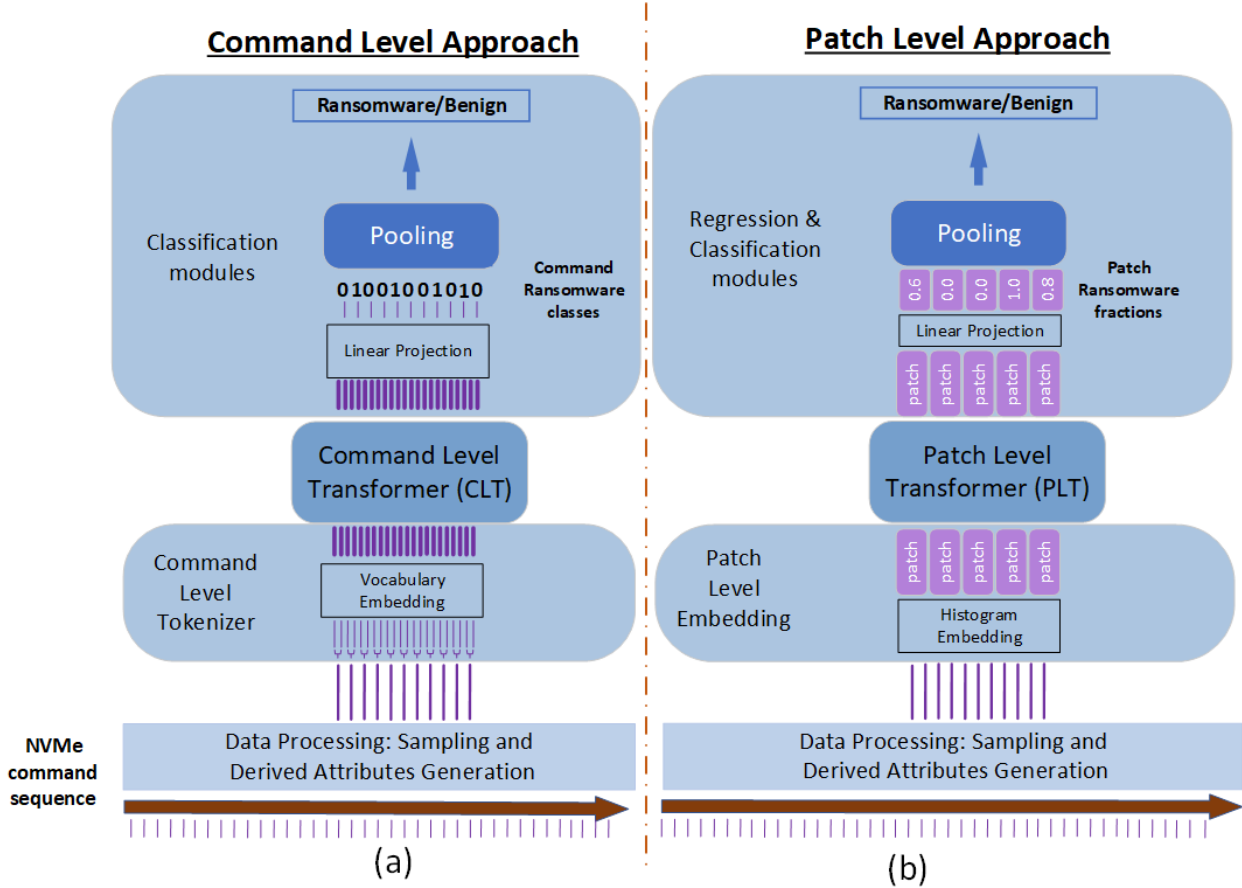


Figure 1: A high-level diagram of our ransomware detection pipelines for both the (a) CLT (left panel) and (b) PLT (right panel) models. Both first sample and process a set of commands from the NVMe stream. Then, each tokenizes the commands, feeds the tokens into its model, and outputs a prediction per token. These token predictions are pooled to produce a final binary prediction.

point $timestamp$ denotes the time of command initialization, $opcode$ is a categorical attribute denoting the command operation (read: R or write: W), the integer $size$ is the sum of bytes the command refers to, and the ordinal $offset$ denoting the byte offset on disk (disk addresses in the range $[offset, offset + size)$ constitute the memory space referred to by the command).

2.1 Derived per-command attributes

The very nature of ransomware is to read data, encrypt it, and then destroy the original data. This led several works (e.g. [6]) to calculate the overwritten byte volume and use it as a feature in detection systems. Inspired by such ideas we complement the fundamental NVMe attributes with additional derived features. In particular, for each command c with $opcode(c) = W$, we identify the command c' that is the latest of all earlier commands with $opcode(c') = R$ and that has overlap OV_{WAR} with the bytes of c (for ‘write-after-read’). We also calculate the time-lapse $\Delta t_{WAR}(c) = timestamp(c) - timestamp(c')$ between c and c' . Because we observed ransomware patterns with multiple read and write operations to the same storage location, we calculate three additional overlaps and time lapses that correspond to all other opcode combinations $(opcode(c), opcode(c')) = (R, R), (R, W), (W, W)$. Similar derived attributes were defined in [5]. Finally, we calculate the per-command time difference $\delta t(c) \equiv timestamp(c) - timestamp(c - 1)$ for each command c to keep track of the IO rate.

2.2 Data Sampling

To generate samples for train and test we sample data by slicing each NVMe stream into successive non-overlapping units of data slices. There are three natural options to define the slices, by equal (i) time extent, (ii) number of commands, or (iii) byte volume. A common choice in the literature is to use option (i) with a time extent of $\sim 10 - 60$ seconds (e.g. [3, 7, 5, 8]). Because the SotA models as well as some of our models can perform detection only after at least one data slice is complete, the earliest detection with option (i) at a typical I/O throughput of 130MB/sec can happen after over a gigabyte of data was read/overwritten by ransomware. To avoid this issue and the potential lack of robustness to throughput variability, we choose to sample with option (ii) and a slice size of 16500 commands or option (iii) with a slice size of 0.5GiB. For brevity, we term the models that are based on slicing options (ii) and (iii) as `ByCommand` and `ByVolume` version models.

3 Models

The structure of our problem requires us to identify the presence of malicious commands, often interspersed with differing amounts of benign commands in between. Any single command or small patch of commands in itself is very hard to model, and it is only when taken with other relevant commands that we can attempt to classify it. Attention mechanism, with its ability to identify relevant information at varying, and often long, distances, and ignore large amounts of irrelevant information in between, is a natural choice for this problem.¹ The architecture itself follows the encoder parts of the architecture presented in [9], with exact specifications given in Appendix A. In the remainder of this section, we introduce two modeling approaches: at the command level, using the Command Level Transformer (CLT), and at the level of small command patches, using the Patch Level Transformer (PLT).

3.1 The Command Level Transformer

The CLT – depicted in Figure 1a – works on frames of 250 commands, which the tokenization process turns into 500 tokens (for tokenization details see next section). The transformer is made up of three self-attention encoding layers, which follow the architecture presented in [9]. On top of the transformer, we then compose a classification module, comprised of a fully connected projection layer – reducing the output dimension back to 500×1 – and a 2×1 convolution with stride 2, producing 250 outputs. These are fed through a softmax layer to predict a label (ransomware or benign) per input command. Thus, the model predicts the label of each command individually, given its context in the frame. Training loss is binary cross-entropy, applied to each of the 250 predictions. During inference, the per-command predictions are averaged over a slice, and this average is then imposed by a threshold to produce a final binary prediction for the entire slice. Full details of the CLT parameters are in Appendix A.

3.1.1 Command Level Tokenization

Each NVMe command contains 7 numerical attributes of different types, altogether containing up to 40 digits per command. Common tokenization methods (e.g. those presented in [10]) would thus result in dozens of tokens per command, and prohibitively long sequences. Instead, we first compress the commands by quantizing each attribute into a few bits, and then tokenize the compressed representation by concatenating those bits into integer tokens. The quantization process uses domain knowledge² to preserve as much information as possible, and is described in detail in Appendix B. Table 1 specifies the quantization method and the bit output for each attribute.

A simple concatenation of the resulting 18 bits into a single token would result in a 256K vocabulary size, forcing us to hold a large (128MB) embedding table to handle it. With such a large vocabulary, many tokens are never seen during training – over 60% for our training data – which may later result in unpredictable behavior during inference time, when such unseen tokens are encountered. Hence, we split each 18-bit token into two 9-bit tokens and trade effective context length, which is reduced from 500 to 250 commands, for a smaller vocabulary size. To make sure the learning algorithm treats the two tokens differently we add a 10^{th} “index” bit to each token in the pair – $index_1 = 0$ for the first and $index_2 = 1$ for the second – thus fully separating the tokens in the embedding space, at the cost of increasing the vocabulary size to 1024, which still avoids the large vocabulary problems mentioned above.

¹ Attempts with a UNET model – with up to x340 more parameters than the transformers – performed worse than the PLT and CLT, so we omit it from the main paper, presenting it in Appendix A.

²e.g. typical distributions of command *size* and *dt*, typical file sizes and OS file system behavior for *offset* bit choice, etc.

Table 1: Quantization and tokenization of NVMe command. The bits are concatenated into a pair of 9-bit tokens, and an additional 10^{th} bit is added to each token as its index in the pair.

Attribute	Operation	Bits	Attribute	Operation	Bits
δt	$\log N$	4	<i>offset</i>	take MSB	4
<i>size</i>	$\log N$	4	<i>offset</i>	take LSB	2
<i>opcode</i>	None	1	OV_{WAR} , OV_{RAR} , OV_{RAW}	binarize	3
$index_1$	always 0	1	$index_2$	always 1	1

3.2 Patch Level Transformer

The PLT shown in Figure 1b follows the idea of [11] and instead of working on individual commands works on 100 small patches of the command stream – these are the tokens of the PLT described in the next section. The transformer has six transformer encoding layers. As depicted in Figure 1b, it has a final regression and classification module comprised of a linear projection to reduce the output dimension to 100×2 and a sigmoid, predicting two fractions per token representing the read and write ransomware IO volumes in a patch. The model is trained to perform per-token fractional regression [12] with a cross-entropy (CE) loss by summing the CE terms of all 100×2 fractional volumes. To get a final prediction for an entire slice, the fractions are summed per token and the result is pooled by averaging across tokens to provide a ransomware/benign prediction probability. We threshold this probability to obtain a binary class per slice. More details on hyper-parameters are in Appendix A.

3.2.1 Patch Level Embedding

To generate tokens each slice is divided into 100 patches by sliding a window. When we model slices with a uniform number of commands (ByCommand slicing), we choose each patch to contain 250 commands with a stride of 165. When we model slices with uniform byte volume (ByVolume slicing) we choose each patch to have a total *size* of 50MB with stride $\simeq 5MB$.

Distinct from the embedding method of [11] and because each command is coupled with attributes of different value types, we find that a natural way to embed the patch data is by quantizing attributes into discrete bins and calculating histograms across commands of certain types (read/write/write-after-read/read-after-read). Further details about this histogram embedding are in Table 2, where we denote by *WAR* and *RAR* commands with $OV_{WAR} > 0$ and $OV_{RAR} > 0$ respectively, and by *Rest* the commands with no such overlaps. Some of the histograms are weighted by *size* or by *OV*. This weighting is chosen to reflect the fact that most ransomware commands carry high *size* because they aim to read and write as fast as possible, thereby enhancing the impact of such commands. Finally, to avoid over-fitting to patterns on certain disk locations we normalize the *offset* values in a slice to zero mean and unit variance, and to increase robustness to throughput variability, we normalized δt and Δt by factors that represent their exponentially back averages across past slices.

In addition, to easily capture information about the total byte size and amount of commands in each patch, we calculate these for read, write, *WAR*, and *RAR* commands, as well as for all command types together. We normalize these additional 9 features to the range $[0, 1]$, and concatenate them to the rest, forming a $d_{input} = 181$ -dimensional embedding space per token. Further details appear in Appendix B.

4 Related work

4.1 Ransomware Defense using Storage I/O Attributes

Almost all research we are aware of combines I/O features with data at the file-system, process, and byte-data levels. For example, works like [13, 6, 14, 15, 4] use a variety of I/O features like the number of bytes read, written, and

Table 2: Details of patch tokens embedding. The *offset* and δt histograms are weighted by *size* and the histograms for Δt_{WAR} and Δt_{RAR} by OV_{WAR} and OV_{RAR} respectively.

NVMe attribute	Histogram Weight	Commands types	Bins
$\log size$	-	read/write/ <i>Rest</i>	12
$\log OV$	-	<i>WAR, RAR</i>	12
<i>offset</i>	<i>size</i>	read/write	14
		<i>WAR, RAR, Rest</i>	14
Δt	<i>OV</i>	<i>WAR, RAR</i>	14
δt	<i>size</i>	Any	14

overwritten, file-level features such as file-type and file-path diversity or patterns in directory transversal. Some also use the written byte entropy, and the similarity between the read and overwritten data. Algorithms in these earlier works were mostly rule-based algorithms (the exception is logistic regression in [15]). More advanced tabular methods were used in [3, 16] where IO and entropy features were calculated from time windows a few seconds wide, fed into a Decision Tree to generate predictions later aggregated along wider time windows. In [17] and [7] the authors add more I/O features and train a Random Forest (RF), an SVM, and a KNN model at granularity of tens of seconds. An RF was also used in [18] applied to higher OS data at the process ID granularity, and [19] used a Decision Tree. More recently, an XGBoost [20], was used in [5] to form the DeftPunk model using features like the IO size, IO byte, IOPS, and *offset* statistics for different types of commands (read, write, overwrite, multi-read, etc.). XGBoost was also used in [8] with entropy, I/O, and file-level features, calculated from a window a few seconds wide.

The data used in the majority of works involves between 1–15 families of ransomware (see [15, 3, 4, 16, 7, 18, 19, 5]) with the exception of [6] using 29 families and [21] using 32. The total volume read or written in [17] and [5] at 9 terabyte and 12 terabyte respectively. None of these published data sets is labeled at the command level making it impossible for us to use.

The SotA ransomware detection algorithms we compare to are tabular models. Due to the lack of published code, we developed a Random Forest (RF) model to represent a typical tabular approach in the literature, inspired by [3]. It is designed to capture patterns in *size*, OV_{WAR} , and Δt_{WAR} , and uses several aggregated features per slice. The second model is DeftPunk which we also implement in code. For further details on the RF and DeftPunk, we refer to Appendix A.

4.2 Token Level Objective with Transformers

Our training tasks are per-token classification and regression. Similar per-token tasks can be found both in the NLP and the Computer Vision literature. Especially, Named Entity Recognition (NER) is, by construction, a token-level classification task and is closest to the task our CLT performs. To our knowledge, it was first benchmarked by a transformer in [22] via fine-tuning – see also the recent [23], the review on NER in [24], and the recent idea in [25], where the problem is treated as a generative few shot learner. A similar task to what our PLT does is described for object recognition in [26]. There, image tokens densely participate in the classification objective by optimizing the sum of the per-token cross-entropies and the class token cross-entropy. This approach is also natural in image segmentation as done by [27] with BERT.

5 Experiments

We experiment with the PLT and the CLT, comparing them to the SotA represented by two models: the RF and DeftPunk which we discuss at the bottom of Section 4.1.

5.1 The Data set

Our experiments are performed on a data set we collect, which we annotated as benign or ransomware at the command level. It contains 1,464 streams with ransomware generated by 137 ransomware variants from 49 ransomware families, encrypting victim data generated in-house and from the NapierOne mixed file benchmark, which is specially designed for ransomware research [28]. It also contains benign streams: in-house generated (575 streams) as well as streams downloaded from 3 subsets of the data curated by Storage Networking Industry Association (SNIA) [29, 30, 31] (686 streams). We randomly choose 2/3 of the streams for train and leave the rest for evaluation. In total, our data set contains over 5×10^9 IO commands that reflect the processing of more than 177 terabytes of data traffic. This is significantly larger than other sets in the literature both in size and in malware coverage. For a detailed description of our data see Appendix C.

5.2 Performance Metrics and Evaluation Method

We measure performance by calculating three types of metrics. The first includes the missed detection rate (MDR), the false alarm rate (FAR), and the $F1$ score: $F1 = 2 \frac{\text{Precision} \times \text{Recall}}{\text{Precision} + \text{Recall}}$. The second involves the volume of megabytes *written* by the ransomware before its first detection by the model – used as a measure of the severity of the damage it caused before being detected. We denote this quantity by MBD (MegaBytes to Detection). In particular, we measure the cumulative distribution function (CDF) of the MBD across all evaluation streams containing ransomware and quote its third upper quantile, MBD_3 . The last type of metrics consists of the percentage P_{miss} of ransomware IO traffic (in megabytes) missed by the model, and the percentage P_{err} of benign IO traffic (in megabytes) erroneously detected as malicious.

All the reported metrics are from the evaluation set and are calculated by cross-validation as follows: we randomly divide the NVMe streams in the evaluation set into validation/test at a ratio of 1:2, set the model thresholds on the prediction probabilities on the validation set, measure performance on the test set, and repeat this process $\times 50$ times. The errors we quote represent the cross-validation 1σ , and for the MDR and the FAR , we also take into account the binomial error. All models were calibrated to the same work point by choosing the FAR to correspond to an average of a single false alarm for every 50GB of benign IO traffic.

We compare the performance of 2 versions of models – `ByCommand` and `ByVolume` (defined by the corresponding data slicing method discussed in Section 2.2). We make sure that all slices in a certain version are identically the same, allowing us to unambiguously compare the MDR , FAR , and $F1$ within each version. In addition, and since MBD_3 , P_{miss} , and P_{err} , are slicing-method agnostic (as they measure volume, which is independent of slicing), we can compare their measurements across versions.

5.3 Main Results

We benchmark a total of 8 models: four from the `ByCommand` version and four from `ByVolume`. In each version, we trained four models of the following types: a PLT, a CLT, and two SotA models – a Random Forest (RF) model and a DeftPunk model. Table 3 reports the comparison of the MDR , $F1$, and MBD_3 for all models.

We choose the optimal model from each type according to the values of the MBD_3 and obtain the `ByCommand` CLT and the `ByVolume` RF, DeftPunk and PLT. We find that the P_{err} for all these is consistent at $P_{err} = 0.6\% - 0.9\%$ with an error of $0.2\% - 0.3\%$ and present P_{miss} and MBD_3 in Table 4.

From Table 3 we see that the two tabular models have similar performance with DeftPunk slightly better than the RF in most metrics and moderately better in P_{miss} . We therefore compare the CLT and PLT to DeftPunk henceforth. We find that the CLT is the superior model in all metrics for both model versions: it is better than DeftPunk by up to $24.4\% \pm 11.0\%$ in MDR , up to $5.8 \pm 1.3\%$ in $F1$, and up to $73.5 \pm 5.3\%$ in MBD_3 . The PLT is also superior to DeftPunk by up to $7.0 \pm 1.2\%$ in $F1$, and up to $44.3 \pm 9.3\%$ in MBD_3 . The PLT also has a better (lower) MDR score compared to DeftPunk but it is below the statistical error. In terms of P_{miss} we find that the PLT is superior to all models and that it is $84.3 \pm 4.1\%$ better than DeftPunk while the CLT is $70.0 \pm 11.0\%$ better.

Finally, we plot the CDF of the MBD in Figure 2 for the models in Table 4. The improvement in MBD_3 is also clear if we inspect Figure 2 where we see that the CLT is very good in terms of detecting ransomware fast, but is prone to a non-negligible tail at very high MBD values. In contrast, the PLT can prevent these situations but is not as good as the CLT at low values of MBD . Both models are superior to the tabular models which are themselves similar.

Table 3: Results for the missed detection rate (MDR) and the $F1$ metrics in percentages, and for the MBD_3 – which is a primary data loss metric – in megabytes. The two parts of the table present results for the `ByCommand` and `ByVolume` version models.

BYCOMMAND	MDR	F1	MBD_3
RF	19.7±2.1	89.9±1.2	335± 53
DEFTPUNK	16.5±1.8	90.8±1.0	366± 58
PLT	14.9±1.7	91.8±0.9	207±100
CLT	12.5±1.1	93.2±0.7	107± 5
BYVOLUME	MDR	F1	MBD_3
RF	22.6±2.3	87.1±1.4	286±33
DEFTPUNK	20.4±2.0	88.4±1.2	282±34
PLT	17.4±1.2	90.3±0.7	157±18
CLT	16.5±1.2	90.8±0.6	97±12

Table 4: Measurements of P_{miss} and of MBD_3 for the optimal models we benchmarked.

MODEL	VERSION	P_{miss}	MBD_3
RF	BYVOLUME	9.0±1.8	286±33
DEFTPUNK	BYVOLUME	6.7±1.1	282±34
PLT	BYVOLUME	1.1±0.2	157±18
CLT	BYCOMMAND	2.0±0.7	97±12

5.4 Robustness to Unseen Ransomware

We now analyze the ability of our models to generalize to unseen ransomware. Since differently named ransomware may in actuality be similar in their behavior, we would like to ensure that we do not have data leaks due to similar ransomware misclassified as unseen. To achieve this we first perform a clustering analysis of the 137 ransomware variants we have in our data set. As a distance metric we use TLSH [32] with a similarity score of 100 [33]. The analysis shows that the actual number of independent ransomware types in the data set is 47, of which 29 are singleton clusters and 9 contain 5 or more ransomware variants. The full list of clusters appears in Appendix C.

We now divide the ransomware variants into 3 roughly equal groups and perform 3 test iterations. For each iteration, we mix two groups and evenly split them into train and in-distribution test sets. The third group is the out-of-distribution test set. The benign streams train and test data remain the same throughout, to provide the same negative samples to the different id and ood tests. We train the models on the train set and test on the id and ood test sets. Finally, we average the results of all three runs and present them in Figure 3.

We see that while there is a visible and statistically significant performance degradation on the ood set, for all models, the PLT and CLT models still perform better than the SotA. In fact, we observe that the ood performance of our models is still better than the id performance of the SotA.

5.5 Per-Token Accuracy

We also find that the results within each data slice are accurate. For example, the PLT-predicted per-token read and write volume of data that is accessed by ransomware exhibits excellent accuracy – see Figure 4 for the cross-token histogram of the correlation between the per-token IO volume written by ransomware and its PLT-predicted value. When we calculate the accuracy of the PLT prediction we find the error in read and write volumes of data accessed by ransomware is at most 4.3MB and 5.5MB for 95% of the 110K ransomware PLT tokens in the evaluation set.

Good within-slice accuracy is also seen for the CLT. To demonstrate this we calculated the prediction accuracy per slice (the fraction of commands in a slice whose label – ransomware or benign – is predicted correctly) and plot it in Figure 5. We group the slices by the actual fraction of ransomware commands they contain and measure the model’s average accuracy on each such group. From the plot, we see that the model accurately predicts, with $\geq 80\%$ accuracy,

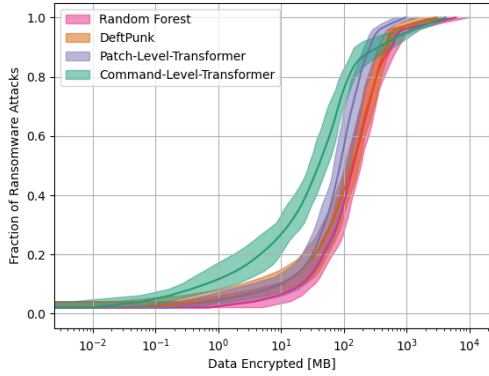


Figure 2: The cumulative distribution function of the MBD for the four best models that appear in Table 4, with their 1σ spread.

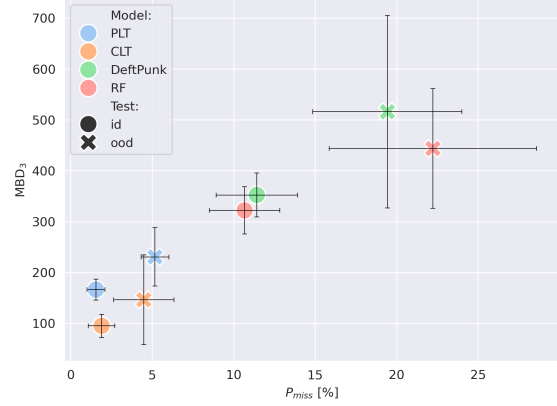


Figure 3: The in-distribution (id) and out-of-distribution (ood) results for MBD_3 and P_{miss} . The error bars take into account both results variability between folds and individual fold uncertainty.

even for the most challenging slices whose ransomware fraction is ~ 0.5 , i.e. that contain about equal amounts of benign and ransomware commands, interspersed among each other. Nevertheless, the model can still separate the mix into ransomware and benign commands with significantly better than random accuracy, showing command-level pattern recognition capabilities. These analyses support our claim that the models do indeed learn low-level patterns in the data, and do not simply revert to some global aggregated function applied equally to all of their outputs.

5.6 The Importance of Context

As discussed above, it is very unlikely that a single command can be modeled well on its own since only its appearance within the context of other commands can determine its origin. Thus, providing sufficient context was an important consideration in our transformer-based architectural choice for the CLT, and here we explicitly check this line of thought. In particular, we trained a set of models with increasingly large contexts and measured their performance. We plot the results in Figure 6 where it is clear that as the context increases, the performance of the CLT improves. Since the prediction of the CLT is per-command, this means that as the context each command “sees” increases, so

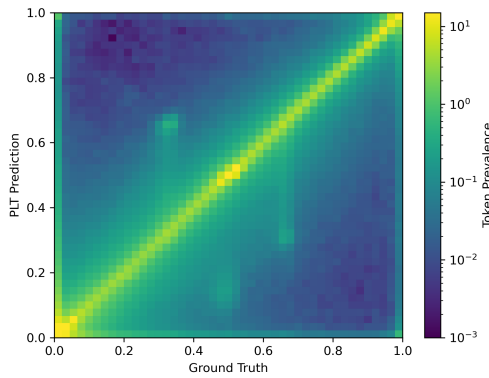


Figure 4: The histogram heatmap for the correlation between the actual fraction of ransomware IO volume and its PLT prediction.

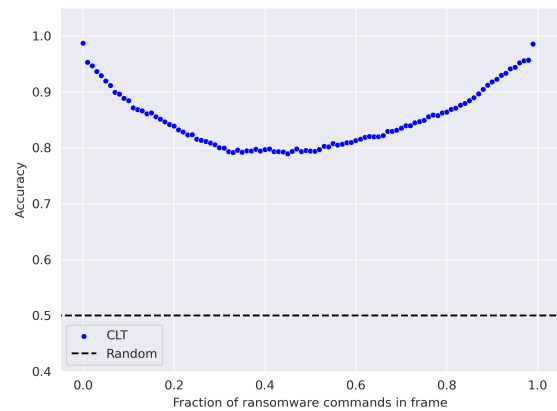


Figure 5: The accuracy of data slices for the CLT versus the slice ransomware command fraction.

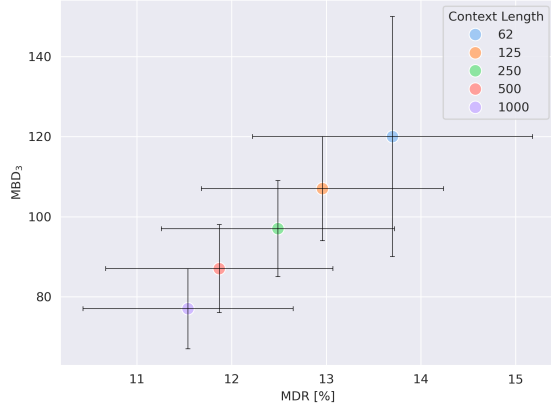


Figure 6: The dependence of MBD_3 and MDR in of the CLT model on the context length. Note that due to splitting each command into two tokens, the actual model input length is twice the numbers shown above.

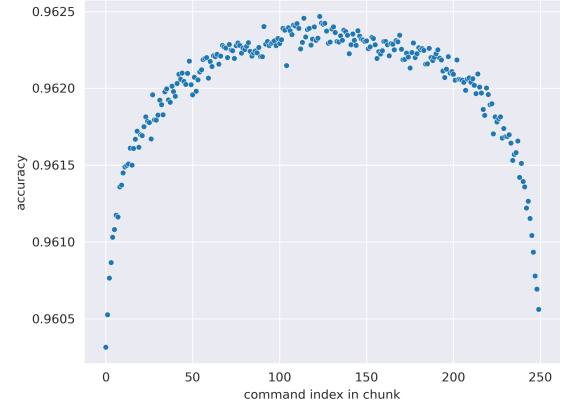


Figure 7: The dependence of command prediction accuracy on its location in the chunk. Commands in the center of the chunk have better prediction accuracy than those on either side of it.

does the model’s ability to correctly predict it. We also note that the CLT model variant we chose – the one trained with $context = 250$, and whose results are presented in Section 5.3 – is not the best in terms of MBD_3 and MDR . Nevertheless, as mentioned below in Section 6 this model was chosen as it is small enough to make it possible to implement in a product.

In Figure 7 we plot the command prediction accuracy as a function of its position in the chunk (calculated over all chunks in the test set). We see that commands in the center of the chunk – i.e. those having at least some context on both sides – are somewhat better predicted on average than those on either side, who have only one-sided context to draw from. While the difference is not large, working on overlapping chunks and taking only the middle 75% of predictions may still improve the overall model performance.

5.7 Feature Ablation

To measure the contribution of our features and tokenization to the overall performance of our models, we measure it for ablated versions of our models’ token space. We do so by training a new set of PLT and CLT models while dropping sub-spaces of the embedding space as per their description in Section 3.1.1 and Section 3.2.1. The results of this study are presented in Table 5. We also test the effect of splitting each of the NVMe commands into two CLT tokens, by training the CLT model on single tokens per command and measuring the results. We find a slight $\times 1.06$ degradation in MBD_3 and the same performance in P_{miss} , assuring us that splitting the command to reduce the vocabulary size does not incur a performance degradation.

6 Hardware Implementation

Our model’s end goal is hardware implementation, especially in SSD devices. Thus, careful considerations must be made to ensure our algorithms can indeed meet the area-on-silicon and throughput requirements of an actual system. As shown in Figure 6, we deliberately chose a smaller, weaker model for the CLT, to make hardware implementation feasible. We discuss the hardware requirements of the full model in Appendix D and below we summarize our findings.

The first requirement one needs to comply with is low DRAM usage, as determined by the number of parameters each model has. The total number of parameters in the CLT is $\sim 450K$ which means it takes up $\sim 1MB$ of DRAM. The PLT is a larger model, with 20M parameters, taking up 40MB of DRAM. Both these DRAM sizes can be accommodated on the internal DRAM of the SSD controller.

The second requirement is that the detection model will be fast enough to keep up with the throughput of the SSD, and we now show that this is indeed the case for our models. Starting with the CLT, we first estimate the number of multiplications it performs in each forward pass at 300M (see Appendix D). Next, assuming that we use 256 multipliers and a clock cycle of 300MHz we observe that a single CLT forward pass takes $\sim 300M/256/300MHz \simeq 4$

Table 5: The results of feature ablation on the CLT and PLT models. Each feature subset was ablated together. The numbers represent the amount by which the corresponding metric increased.

Command Token Ablation			Patch Token Ablation		
Feature Subset	Degradation		Feature Subset	Degradation	
	P_{miss}	MBD_3		P_{miss}	MBD_3
<i>offset</i>	x2.1	x1.6	<i>size</i>	x4.6	x2.3
δt	x1.7	x1.3	δt	x5.1	x2.2
<i>opcode</i>	x1.4	x1.2	fractions	x1.4	x1.2
<i>size</i>	x1.3	x1.1	Δt	x1.2	x1.2
<i>OV</i>	x1.3	x1.1	<i>offset</i>	<1.1	<1.1
<i>index</i>	x1.1	x1.1	<i>OV</i>	<1.1	None

milliseconds. Because such a CLT forward pass processes 250 commands we find that at a typical sequential workload of 256KB per command the corresponding data traffic amounts to $250 \cdot 256K \sim 64MB$. Hence we see that the CLT can support a throughput of $\sim 64MB/4\text{millisecond} = 16\text{GBps}$, well above the throughput of even the fastest SSD drives currently on the market [34]. The corresponding calculation for the PLT proceeds similarly. First, being a larger model it uses 1.8B multiplications in a single forward pass (again see Appendix D), taking up 24milliseconds. Next, the fact that the PTL operates on data slices of 0.5GiB each, means it supports throughput of $0.5\text{GiB}/24\text{milliseconds} = 21\text{GBps}$, again posing no constraint on the implementation.

Finally, since our networks work with half-precision floating point operations, and the area cost of one half-precision multiplier is $\sim 2K$ gates, our total area cost is $\sim 256 \cdot 2K = 512K$ gates, which is an acceptable addition to a modern SSD controller.

6.1 Hardware Versus Software Implementation

In choosing to implement the ransomware detection module into the hardware of the SSD controller we are motivated by several advantages, compared to software implementations.

The first advantage is high computational efficiency. As shown in the previous section, our use of hardware parallelization allows us to keep up with the required SSD throughput. In contrast, we observe that processing in software with a dedicated CPU core operating at 3GHz would lead to an approximate $\times 25$ slow-down compared to the hardware implementation, and to significant latency effects. A second advantage is resistance to malware interference: while software-based solutions may be disabled by the attacking malware, solutions implemented into the SSD controller cannot be affected by such external software processes, and so are immune to attacks, and cannot be turned off or disrupted by malware. A third advantage of our SSD-based solution is that its garbage collection naturally allows one to recover lost data even when it has been deleted at the software level, thus enabling full data recovery even for data corrupted by the ransomware before it was detected.

These advantages and the fact that any other hardware-based solutions require the addition of specialized hardware modules to the storage system – increasing form factor, cost, and complexity – make our implementation into the hardware of the SSD controller a very natural and comprehensive solution.

7 Limitations

The large amount of calculations our models perform increases their on-chip area requirements compared to SotA models such as the RF or DeftPunk. This entails that for very low-resource systems (e.g. phones), our models would require additional work to be competitive with current SotA models. Thus our product is currently intended for medium to high-resource systems (e.g. SSDs and data storage servers), and future work will improve our models to support low-resource systems as well.

8 Summary

In this paper, we take a novel approach to the problem of detecting ransomware activity by inspecting the NVMe IO stream. We reformulate the problem, moving away from aggregative statistical features and instead work with the NVMe stream directly, making use of its sequential nature. For this purpose, we first devise a method of converting our raw data into tokens and then employ the transformer architecture which, as we show, is uniquely suited to the specific characteristics of our data. We further demonstrate that our models learn to classify individual commands in their context and measure ransomware activity within small patches of commands, even when presented with a difficult mixed stream. We also show that context matters – the more context a command “sees”, the better its prediction will be.

We compare our approach against SotA methods using classification metrics as well as metrics designed to measure ransomware damage, and see that our models’ performance is superior to theirs and that this advantage is robust; preserved even when our models are tested on ransomware variants that are out of distribution and never seen during training. We also show that we could further improve the performance of our model by increasing its context length, but by taking instead the variant we presented, our solution becomes viable for inclusion in SSD products.

References

- [1] Harun Oz, Ahmet Aris, Albert Levi, and A. Selcuk Uluagac. A survey on ransomware: Evolution, taxonomy, and defense solutions. *ACM Comput. Surv.*, 54(11s), September 2022. ISSN 0360-0300. URL <https://doi.org/10.1145/3514229>.
- [2] Jamil Ispahany, Md. Rafiqul Islam, Md. Zahidul Islam, and M. Arif Khan. Ransomware detection using machine learning: A review, research limitations and future directions. *IEEE Access*, 12:68785–68813, 2024.
- [3] SungHa Baek, Youngdon Jung, Aziz Mohaisen, Sungjin Lee, and DaeHun Nyang. Ssd-insider: Internal defense of solid-state drive against ransomware with perfect data recovery. In *2018 IEEE 38th International Conference on Distributed Computing Systems (ICDCS)*, pages 875–884, 2018.
- [4] Peiying Wang, Shijie Jia, Bo Chen, Luning Xia, and Peng Liu. Mimosaftl: Adding secure and practical ransomware defense strategy to flash translation layer. In *Proceedings of the Ninth ACM Conference on Data and Application Security and Privacy, CODASPY ’19*, page 327–338, New York, NY, USA, 2019. Association for Computing Machinery. ISBN 9781450360999. URL <https://doi.org/10.1145/3292006.3300041>.
- [5] Zhongyu Wang, Yaheng Song, Erci Xu, Haonan Wu, Guangxun Tong, Shizhuo Sun, Haoran Li, Jincheng Liu, Lijun Ding, Rong Liu, Jiayi Zhu, and Jiasheng Wu. Ransom access memories: Achieving practical ransomware protection in cloud with DeftPunk. In *18th USENIX Symposium on Operating Systems Design and Implementation (OSDI 24)*, pages 687–702, Santa Clara, CA, July 2024. USENIX Association. ISBN 978-1-939133-40-3. URL <https://www.usenix.org/conference/osdi24/presentation/wang-zhongyu>.
- [6] Amin Kharraz and Engin Kirda. Redemption: Real-time protection against ransomware at end-hosts. pages 98–119, 10 2017. ISBN 978-3-319-66331-9.
- [7] Manabu Hirano, Ryo Hodota, and Ryotaro Kobayashi. Ransap: An open dataset of ransomware storage access patterns for training machine learning models. *Forensic Science International: Digital Investigation*, 40: 301314, 2022. ISSN 2666-2817. URL <https://www.sciencedirect.com/science/article/pii/S2666281721002390>.
- [8] Nicolas Reategui, Roman Pletka, and Dionysios Diamantopoulos. On the generalizability of machine learning-based ransomware detection in block storage, 2024, 2412.21084. URL <https://arxiv.org/abs/2412.21084>.
- [9] Ashish Vaswani, Noam Shazeer, Niki Parmar, Jakob Uszkoreit, Llion Jones, Aidan N. Gomez, Łukasz Kaiser, and Illia Polosukhin. Attention is all you need. In *Proceedings of the 31st International Conference on Neural Information Processing Systems, NIPS’17*, page 6000–6010, Red Hook, NY, USA, 2017. Curran Associates Inc. ISBN 9781510860964.

- [10] Aaditya K. Singh and DJ Strouse. Tokenization counts: the impact of tokenization on arithmetic in frontier llms, 2024, 2402.14903. URL <https://arxiv.org/abs/2402.14903>.
- [11] Alexey Dosovitskiy, Lucas Beyer, Alexander Kolesnikov, Dirk Weissenborn, Xiaohua Zhai, Thomas Unterthiner, Mostafa Dehghani, Matthias Minderer, Georg Heigold, Sylvain Gelly, Jakob Uszkoreit, and Neil Houlsby. An image is worth 16x16 words: Transformers for image recognition at scale. *CoRR*, abs/2010.11929, 2020, 2010.11929. URL <https://arxiv.org/abs/2010.11929>.
- [12] Esmeralda A. Ramalho, Joaquim J.S. Ramalho, and José M.R. Murteira. Alternative estimating and testing empirical strategies for fractional regression models. *Journal of Economic Surveys*, 25(1):19–68, 2011. <https://onlinelibrary.wiley.com/doi/pdf/10.1111/j.1467-6419.2009.00602.x>. URL <https://onlinelibrary.wiley.com/doi/abs/10.1111/j.1467-6419.2009.00602.x>.
- [13] Manish Shukla, Sutapa Mondal, and Sachin Lodha. Poster: Locally virtualized environment for mitigating ransomware threat. In *Proceedings of the 2016 ACM SIGSAC Conference on Computer and Communications Security, CCS '16*, page 1784–1786, New York, NY, USA, 2016. Association for Computing Machinery. ISBN 9781450341394. URL <https://doi.org/10.1145/2976749.2989051>.
- [14] Joon-Young Paik, Joong-Hyun Choi, Rize Jin, Jianming Wang, and Eun-Sun Cho. A storage-level detection mechanism against crypto-ransomware. In *Proceedings of the 2018 ACM SIGSAC Conference on Computer and Communications Security, CCS '18*, page 2258–2260, New York, NY, USA, 2018. Association for Computing Machinery. ISBN 9781450356930. URL <https://doi.org/10.1145/3243734.3278491>.
- [15] Donghyun Min, Donggyu Park, Jinwoo Ahn, Ryan Walker, Junghee Lee, Sungyong Park, and Youngjae Kim. Amoeba: An autonomous backup and recovery ssd for ransomware attack defense. *IEEE Computer Architecture Letters*, 17(2):245–248, 2018.
- [16] Sungha Baek, Youngdon Jung, David Mohaisen, Sungjin Lee, and DaeHun Nyang. Ssd-assisted ransomware detection and data recovery techniques. *IEEE Transactions on Computers*, 70(10):1762–1776, 2021.
- [17] Manabu Hirano and Ryotaro Kobayashi. Machine learning-based ransomware detection using low-level memory access patterns obtained from live-forensic hypervisor. In *2022 IEEE International Conference on Cyber Security and Resilience (CSR)*, pages 323–330, 2022.
- [18] Kosuke Higuchi and Ryotaro Kobayashi. Real-time defense system using ebpf for machine learning-based ransomware detection method. In *2023 Eleventh International Symposium on Computing and Networking Workshops (CANDARW)*, pages 213–219, 2023.
- [19] Weidong Zhu, Grant Hernandez, Tian Dave (Jing) Garcia, Washington, Sara Rampazzi, and Kevin Butler. Minding the semantic gap for effective storage-based ransomware defense. In *International Conference on Massive Storage Systems and Technology*, 2024.
- [20] Tianqi Chen and Carlos Guestrin. Xgboost: A scalable tree boosting system. In *Proceedings of the 22nd ACM SIGKDD International Conference on Knowledge Discovery and Data Mining, KDD '16*, page 785–794, New York, NY, USA, 2016. Association for Computing Machinery. ISBN 9781450342322. URL <https://doi.org/10.1145/2939672.2939785>.
- [21] Boyang Ma, Yilin Yang, Jinku Li, Fengwei Zhang, Wenbo Shen, Yajin Zhou, and Jianfeng Ma. Travelling the hypervisor and ssd: A tag-based approach against crypto ransomware with fine-grained data recovery. In *Proceedings of the 2023 ACM SIGSAC Conference on Computer and Communications Security, CCS '23*, page 341–355, New York, NY, USA, 2023. Association for Computing Machinery. ISBN 9798400700507. URL <https://doi.org/10.1145/3576915.3616665>.
- [22] Jacob Devlin, Ming-Wei Chang, Kenton Lee, and Kristina Toutanova. BERT: Pre-training of deep bidirectional transformers for language understanding. In Jill Burstein, Christy Doran, and Thamar Solorio, editors, *Proceedings of the 2019 Conference of the North American Chapter of the Association for Computational Linguistics: Human Language Technologies, Volume 1 (Long and Short Papers)*, pages 4171–4186, Minneapolis, Minnesota, June 2019. Association for Computational Linguistics. URL <https://aclanthology.org/N19-1423/>.

- [23] Fábio Souza, Rodrigo Nogueira, and Roberto Lotufo. Portuguese named entity recognition using bert-crf, 2020, 1909.10649. URL <https://arxiv.org/abs/1909.10649>.
- [24] Jing Li, Aixin Sun, Jianglei Han, and Chenliang Li. A survey on deep learning for named entity recognition : Extended abstract. In *2023 IEEE 39th International Conference on Data Engineering (ICDE)*, pages 3817–3818, 2023.
- [25] Shuhe Wang, Xiaofei Sun, Xiaoya Li, Rongbin Ouyang, Fei Wu, Tianwei Zhang, Jiwei Li, and Guoyin Wang. Gpt-ner: Named entity recognition via large language models, 2023, 2304.10428. URL <https://arxiv.org/abs/2304.10428>.
- [26] Zihang Jiang, Qibin Hou, Li Yuan, Daquan Zhou, Yujun Shi, Xiaojie Jin, Anran Wang, and Jiashi Feng. All tokens matter: token labeling for training better vision transformers. In *Proceedings of the 35th International Conference on Neural Information Processing Systems, NIPS '21*, Red Hook, NY, USA, 2021. Curran Associates Inc. ISBN 9781713845393.
- [27] Ji He, Lina Zhao, Hongwei Yang, Mengmeng Zhang, and Wei Li. Hsi-bert: Hyperspectral image classification using the bidirectional encoder representation from transformers. *IEEE Transactions on Geoscience and Remote Sensing*, 58(1):165–178, 2020.
- [28] Simon R. Davies, Richard Macfarlane, and William J. Buchanan. Napierone: A modern mixed file data set alternative to govdocs1. *Forensic Science International: Digital Investigation*, 40:301330, 2022. ISSN 2666-2817. URL <https://www.sciencedirect.com/science/article/pii/S2666281721002560>.
- [29] Chunghan Lee, Tatsuo Kumano, Tatsuma Matsuki, Hiroshi Endo, Naoto Fukumoto, and Mariko Sugawara. Systor '17 traces (SNIA IOTTA trace set 4928). In Geoff Kuenning, editor, *SNIA IOTTA Trace Repository*. Storage Networking Industry Association, March 2016. URL <http://iotta.snia.org/traces/block-io?only=4928>.
- [30] Dushyanth Narayanan, Austin Donnelly, and Antony Rowstron. MSR Cambridge traces (SNIA IOTTA trace set 388). In Geoff Kuenning, editor, *SNIA IOTTA Trace Repository*. Storage Networking Industry Association, March 2007. URL <http://iotta.snia.org/traces/block-io?only=388>.
- [31] Vishal Sharda, Swaroop Kavalanekar, and Bruce Worthington. Microsoft production server traces (SNIA IOTTA trace set 158). In Geoff Kuenning, editor, *SNIA IOTTA Trace Repository*. Storage Networking Industry Association, March 2008. URL <http://iotta.snia.org/traces/block-io?only=158>.
- [32] Jonathan Oliver, Chun Cheng, and Yanggui Chen. Tlsh – a locality sensitive hash. In *2013 Fourth Cybercrime and Trustworthy Computing Workshop*, pages 7–13, 2013.
- [33] Haoping Liu, Josiah Hagen, Muqet Ali, and Jonathan Oliver. An evaluation of malware triage similarity hashes. In *ICEIS (I)*, pages 431–435, 2023.
- [34] Jarred Walton. Ssd benchmarks hierarchy 2025. <https://www.tomshardware.com/features/ssd-benchmarks-hierarchy>, 2025. Accessed: 2025-01-23.

A Model Specifications

A.1 Random Forest Model

The first model we use as a baseline comparison for our approach is a Random Forest (RF) with 23 tabular features extending past works on decision trees and random forest approaches like [3]. Especially, to avoid over-fitting and being constrained by the hardware implementation, our model is restricted to 20 trees with a maximum depth of 20. After training (using the Gini criterion) we validated through a feature importance analysis the common wisdom, which suggests the read and overwrite fractional volumes are the most important features (during a ransomware cyber attack, the read, write, and overwrite volumes are nearly identical, making the fractional read and overwrite volume very close to $1/2$). We find that the space on the disk the trained model takes up is roughly $18MB$ corresponding to 260K nodes in the forest.

A.1.1 Features

We recall that the featurization process is preceded by slicing the data into slices of identical read and write volume (option (iii) described in Section 2.2) and that we choose the slice volume to be equal to $V_0 = 0.5GiB$. We extract the features we present in Table 6 from each slice. In that table, we denote by V the total number of logical blocks in the slice. The value of V obeys $V \lesssim V_0$ because there is no guarantee the cumulative sum of *size* along the trace will be evenly commensurate with V_0 . Finally by $\sigma_{OV_{WAR}}$ and $\mu_{OV_{WAR}}$ we denote the standard deviation and the mean of OV_{WAR} across the commands of the slice. We choose 10 bins for the histograms H_R and H_{WAR} described in Table 6 and so have 23 features per slice.

Table 6: RF Features

f_R	$\frac{1}{V} \sum_{opcode=R} size(c)$
f_{WAR}	$\frac{1}{V} \sum_c OV_{WAR}(c)$
CV_{WAR}	$\sigma_{OV_{WAR}}/\mu_{OV_{WAR}}$
H_R	The histogram of read commands' <i>size</i>
H_{WAR}	The histograms of OV_{WAR} values

A.2 DeftPunk Model

The second baseline model we use is the DeftPunk model [5]. It is a two-layer model: the authors choose to apply a Decision Tree (DT) on a first set of features and pass the ransomware-suspicious samples to a second layer chosen to be XGBoost which is applied on a larger set of features. The partition between features in the first and second layers is done by the computational effort made in feature extraction and we follow the same choice described by the authors. The models we trained have a maximum depth of 6 in both the DT and the XGBoost. We found that the model on disk takes up $0.5MB$, corresponding to its 10K nodes, and 100 trees in the XGBoost.

A.3 CLT and PLT Models

We describe the hyperparameters chosen for the CLT and the PLT in Table 7 and Table 8, respectively.

For both models, we used an ADAM optimizer with a learning rate of $1e^{-4}$. The CLT's optimizer used an LRScheduler of 30 steps and $\gamma = 0.8$. The CLT and PLT were trained for 300 and 400 epochs, respectively. Our models' receiver operating characteristic (ROC) thresholds, as calculated on the cross-validation set, are presented in Table 9.

Table 7: CLT Hyperparameters.

Hyperparameter Name	Chosen Value
Vocabulary Size	1,024
Batch Size	64
Embedding Dimensions	128
Feedforward Dimensions	128
No. of Heads	4
No. of Layers	3
Context Length	500
Convolution Kernel Size	2
Dropout	0.1

Table 8: PLT Hyperparameters

Hyperparameter Name	Chosen Value
Input Size	181
Batch Size	256
Embedding Dimensions	512
Feedforward Dimensions	2,048
No. of Heads	4
No. of Layers	6
Context Length	100
Dropout	0.1

A.4 UNET

To test the importance and fit of the transformer architecture we tested other architectures like fully connected applied to a concatenation of the PLT features of all tokens, as well as 1D convolutional networks. The best models of these architectures were of the UNET type with the architecture Appendix A.4.1, input with the tokens of the PLT, hence $T(0) = T(f) = 100$ and $F(0) = 181$ and $F(f) = 2$. The results of the best UNET model are presented in Table 11 together with the result of our PLT and CLT from Section 5. The results demonstrate that the UNET is of a degraded performance compared to the transformer, even for very large models with over x10 parameters.

A.4.1 UNET Architectures

We pictorially present the specific implementation of the architecture we use in Figure 8. By $T(i)$, $F(i)$ we denote the number of tokens and the embedding size respectively of the UNET level i . The blue arrows denote a max pooling with kernel size = 2 which means that $T(i + 1) = T(i) // 2$. The green arrow denotes transpose convolution with stride = 2 and with kernel size equal to $\max(3, k)$, where k is a parameter of the encoder and decoder blocks E and D that we discuss below. This transpose convolution also reduces the embedding dimension $\times 2$. The blocks $B(i)$ denote the concatenation of the UNET skip connection (the dashed arrow) and the result of the transposed convolution along the feature dimension. Finally, the block C denotes a 1×1 convolution from an initial dimension (which after $D(1)$ is

Table 9: Models' ROC Thresholds

Model Name	ROC Threshold
CLT	0.17253 ± 0.03187
PLT	0.136298 ± 0.024286
RF	0.903377 ± 0.017638
DefnPunk	0.964811 ± 0.009038

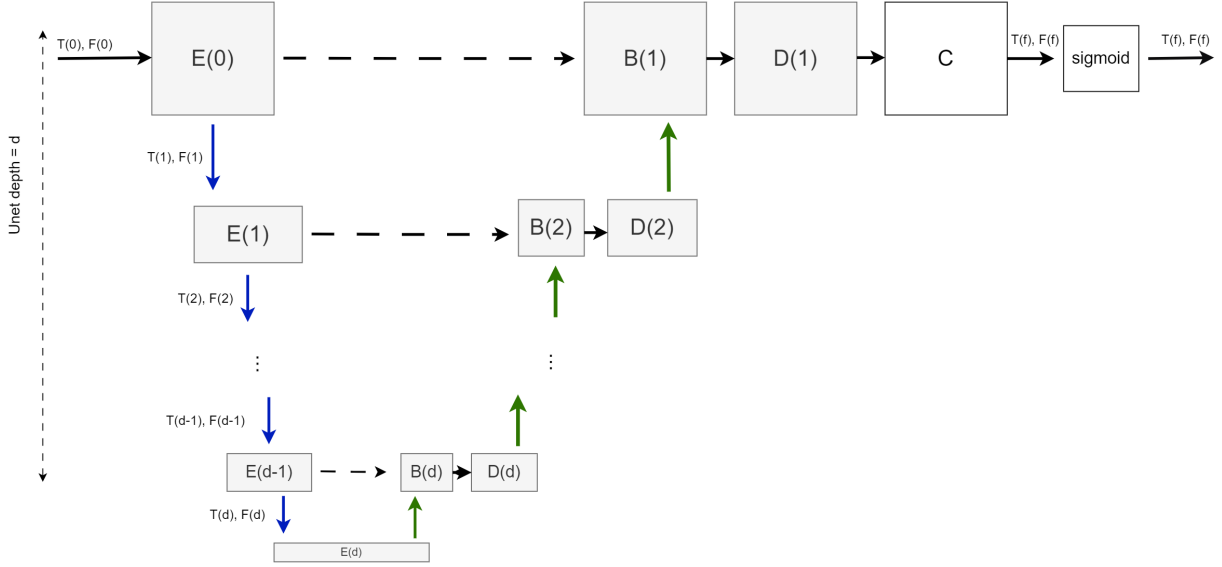


Figure 8: A pictorial representation of the UNET architecture that we use.

equal to $2F(0)$) into a final dimension equal to 2, followed by a sigmoid. This provides an output of dimension $T(0) \times 2$ of elements, each bounded in the range $[0, 1]$, that is then compared to the read-and-write ransomware fractions series using a binary cross entropy loss function.

The *padding* and *output_padding* parameters of the transpose convolutions depend on the value of $T(i)$ (or more precisely on whether $T(i)$, which is determined by applying pooling on the higher-level series with size $T(i-1)$, obeys $T(i-1) = T(i) \times 2$ or $T(i-1) = T(i) \times 2 + 1$). The main UNET parameters are the depth d of the UNET and the kernel size k of the E and D blocks in Table 10 which we grid search for $d = 0, 1, 2, 3$ and $k = 3, 5, 7, 9$ (when the UNET depth is zero, $d = 0$, the architecture represented by the set of gray rectangles in Figure 8 reduces to $E(0)$). The initial dimensions $T(0)$ and $F(0)$ can also be considered as hyper-parameters, but $T(f), F(f)$ are not as we fix them to obey $T(f) = T(0)$ and $F(f) = 2$. We attempted various types of encoder and decoder blocks (the E and D blocks in Figure 8) including ResNet blocks and simple convolutions, and found that the best are those presented in Table 10.

Table 10: The encoder block E and decoder block D .

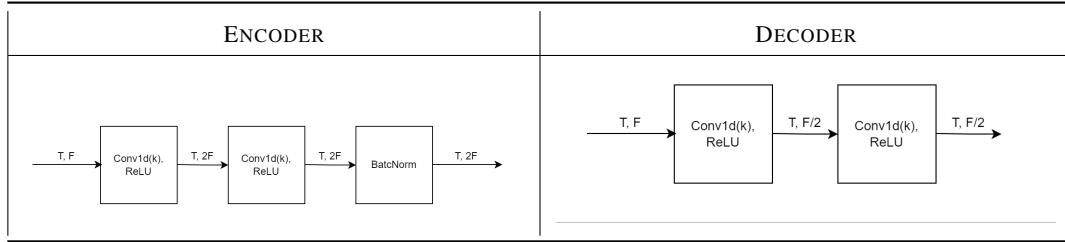


Table 11: Performance of the best architectures. All models were calibrated to have the same work point where the upper limit of the 1σ confidence interval obeys $FAR_{\text{upper}} \leq 1\%$.

Architecture	FAR [%]	MDR [%]	MBD_3	Number of Parameters
CLT	0.77 ± 0.30	12.5 ± 1.1	107 ± 5	0.45M
PLT	0.84 ± 0.21	17.4 ± 1.2	157 ± 18	17M
UNET	0.76 ± 0.26	18.7 ± 1.5	195 ± 41	153M

B Tokenization Specifications

B.1 CLT Tokenization

Each NVMe command, c , passes through the CLT tokenization scheme, as follows:

- $\delta t(c) \equiv \min(\text{round}(\log((\text{timestamp}(c) - \text{timestamp}(c - 1)) \cdot 10^5 + 1)), 15)$.
- $\text{size} \equiv \min(\lfloor \log(\frac{S}{512}) \rfloor, 12)$. Where S is the size of the command in bytes. Since 4 bits are assigned, the remaining 3 bins (13, 14, 15) are assigned to particularly common size values: 512K, 128K, and 16K.
- The command’s opcode (R/W) is assigned with 1 bit.
- The three auxiliary attributes - WAR, RAR, and RAW - are assigned 1 bit each, denoting whether their value for this command is greater than 0.
- The last (minor) 21 bits of the offset are dropped (this represents a 2MB resolution) and the next 2 bits are taken as offset_{lsb} .
- The first (major) 4 bits of the offset are taken as offset_{msb} .

In total, these attributes are spread across two tokens, where each token is composed of 9 bits: the first token contains the $\delta t(c)$, size, and opcode attributes - and the second receives the two offset attributes and the three auxiliary attributes. Then, an additional single-bit is added to each token (0 to the first, 1 to the second), denoting its index in the token pair, and creating a $2^{10} = 1024$ vocabulary size.

B.2 PLT Tokenization

In this section, we detail how we normalize some of our features.

B.2.1 Normalization of δt , Δt , and the offset

Starting with the timestamp related quantities, for each slice I and a per-command attribute Q (for example $Q = \delta t$ or $\Delta t_{W,R}$) we denote by $\langle Q \rangle_{I,w}$ the average across all commands within a slice performed with the per-command weight w_c ,

$$\langle Q \rangle_{I,w} = \frac{\sum_{c \in I} Q_c w_c}{\sum_{c \in I} w_c}, \quad (1)$$

and by $\langle\langle Q \rangle\rangle_{I,w}$ the exponentially back averaged of $Q_{I,w}$ across slices, defined recursively by $\langle\langle Q \rangle\rangle_{I,w} = \alpha \langle\langle Q \rangle\rangle_{I-1,w} + (1 - \alpha) \langle Q \rangle_{I,w}$. In this work, we choose the diminishing factor $\alpha = 0.8$, which means the effective memory of the average is $\sim 1 / \log \alpha^{-1} \sim 4.48$ slices. For featurization, we define the following normalized quantities.

$$\overline{\text{offset}}_I \equiv (\text{offset} - \langle \text{offset} \rangle_{I, \text{size}^2}) / \sqrt{\langle \text{offset}^2 \rangle_{I, \text{size}^2}}, \quad (2)$$

$$\overline{\delta t}_I \equiv \delta t / \langle \langle \delta t \rangle \rangle_{I, \text{size}^2}, \quad (3)$$

$$\overline{\Delta t}_I \equiv \Delta t / (10 \langle \langle \delta t \rangle \rangle_{I, OV^2}). \quad (4)$$

The purpose of the δt normalization is to create an embedding that is invariant to CPU speed while normalizing the size is aimed to achieve a disk size invariant embedding.

B.2.2 Normalization of per-token IO size and IO byte

As mentioned in Section 3.2.1 we concatenate to the histogram features of Table 2 a set of 9 features associated with the number and volume of commands in a patch token. We describe their normalization in Table 12 and Table 13. Here the normalization factors v_0 and n_0 are the designed token width in the `ByVolume` and `ByCommand` version models and were chosen as $v_0 = 50MB$ and $n_0 = 250$.

Table 12: The details of the last 9 features participating in the token embedding for the `ByVolume` PLT.

Feature	Normalization factor	Number of features
Patch volume	v_0	1
Patch read and write volume	v_0	2
Sum of OV_{WAR} and OV_{RAR} in a patch	v_0	2
Number of read/write commands in a patch	Number of commands in a patch	2
Number of WAR and RAR commands in a patch	Number of commands in a patch	2

Table 13: The details of the last 9 features participating in the token embedding for the `ByCommand` PLT.

Feature	Normalization factor	Number of features
Patch number of commands	n_0	1
Patch read and write number of commands	n_0	2
Number of WAR and RAR commands in a patch	n_0	2
The volume of read/write commands in a patch	Patch volume	2
Sum of OV_{WAR} and OV_{RAR} in a patch	Patch volume	2

C Data Specifications

C.1 Specification of the data set used

Our data set was collected with a data collection, verification, and labeling system, that we developed in-house. Additional information on the data set is brought in Table 14. In particular, we ran 49 ransomware variants list in Table 15. We also ran 17 types of benign software that are presented in Table 16.

These ran on virtualization of stand-alone PCs with either a 100GB SSD whose disk usage was up to 95%, or a 512GB SSD disk with a disk usage of 49%-60%. The OS was a Windows 10h22 home edition, with two CPUs: Intel(R) Core(TM) i9-10900F and i9-11900K, and with 16GB RAM. In addition, we placed different types of victim files on the virtual disk, including the Napier-Small repository (157GB) and the Napier-tiny repository (17.8GB) [28], some from an in-house generic user files repository, and 57GB stored in $\sim 65K$ png files from the DiffusionBM-2M data set repository. Finally, because we saw that disk indexing can be a CPU-heavy process and can significantly change the NVMe sequence, the data was generated in two configurations: where the indexing processes are either turned on or off. In total, we collected data from 6 such configurations. Each of our traces reflects up to approximately 1000 seconds of operation time, with additional variability introduced via varying the launch time of ransomware. The description of the images on which we ran the workloads is brought in Table 17.

Table 14: Data set Overview

Label	Number of Recordings			Volume [TiB]			Hours	No. of Commands
	Train	Test	Total	Train	Test	Total		
Ransomware	971	493	1,464	89.6	45.05	134.65	402.7	3,896,418,082
Benign	882	379	1,261	29.4	12.96	42.36	1930	1,339,832,788
Total	1,853	872	2,725	119	58.01	177.01	2332.7	5,236,250,870

C.2 Details for Clustering and Robustness Analysis

For each experiment of the leave-one-out cross-validationSection 5.4, the data set was partitioned into three folds. Each fold represents the data used for an out-of-distribution test set and is presented in Table 18. Each ransomware variant is named in the format FAMILY_ABCD stating the ransomware family name and the first four characters of the SHA-256 hash commonly used as the ransomware signifier.

The TLSH distance chosen for the clustering process was 100 (every distance between 50 to 100 yielded the same clusters). In rows where more than one cluster (of the same size) appears, the different clusters are distinguished and separated from one another with round brackets.

Table 15: Ransomware families in our data set

Ransomware Families	No. of Variant Streams per Family
Sodinokibi	14
LockBit	9
BlackMatter	8
Hive, Thanos	7
AvosLocker	6
Maze, BlackBasta, TimeTime, Babuk	5
Mespinoza, RagnarLocker, GlobeImposter	4
Play, Karma, Lorenz, Diavol	3
Sugar, WannaCry, MedusaLocker, Royal, ViceSociety, Stop, Cuba, Rook, Conti, BianLian	2
Neshta, CryLock, Zeppelin, Ransomware.Makop, Alkhal, Clop, LIKEAHORSE, Teslarvng, ATOMSILO, Ransomware.Koxic, Phobos, RansomEXX, RanzyLocker, Nefilim, MRAC, Intercobros, HelloXD, DECAF, MountLocker, BlackOut, Cerber, DarkSide	1

Table 16: Benign SW workload types. Additional variability was introduced by using more than a single parameter for certain SWs. For example, the files read, written, deleted, archived, and encrypted were varied.

Workload Type	Specific Application
Archiving	7z, winRAR
Encryption	AESCrypt
Deletion	SDelete, fsutil
Other disk accesses	download and install apps from the internet git clone read and write files from disk conda install, pip install Windows update Compilation Document editing Web surfing Application downloading and installing Disk populating

Table 17: Disk images

SSD Volume [GB]	Victim File Sources	Disk Occupancy	No. of Images
100	Napier, 65K png files from the DiffusionBM-2M data set repository, a user file collection	10% - 95%	3
512		50% - 60%	

Table 18: Ransomware variant divided into clusters per fold.

Ransomware Variant Clusters	Cluster Size	Number of Clusters	Fold
AvosLocker_43b7, Ransomare.Koxic_7a5e, Mespinoza_44f1, AvosLocker_fb54, Mespinoza_7c77, Mespinoza_f602, Mespinoza_0433, Neshta_9317, Cerber_078d, AvosLocker_f810, AvosLocker_6cc5, AvosLocker_c0a4, AvosLocker_84d9, Conti_24ac, RansomEXX_fa28, BlackBasta_2558, Lorenz_1264, Lorenz_a0cc, Lorenz_edc2, Teslarvng_bb91	20	1	1
TimeTime_5ee8, TimeTime_972e, TimeTime_b599, TimeTime_b722, Royal_44f5, Royal_d9be,	6	1	
Babuk_eb18, Babuk_ca0d, Babuk_575c, Babuk_a522, Babuk_77c7	5	1	
Karma_4dec, Karma_3462, Karma_84d2	3	1	
Cuba_21ac, BlackBasta_723d	2	1	
ViceSociety_HelloKitty_fa72, Alkhal_7a31, ATOMSILO_d9f7, Stop_0d50, Sugar_09ad, Maze_4263, MRAC_768c, Phobos_265d, WannaCry_be22, Play_952f	1	10	
Sodinokibi_fd16, Sodinokibi_b992, Sodinokibi_0441, Sodinokibi_6834, Sodinokibi_20d4, Sodinokibi_9df3, Sodinokibi_de20, Sodinokibi_9b11, Sodinokibi_cb4a, Sodinokibi_2f00, Sodinokibi_9437, Sodinokibi_7c8c, Sodinokibi_db59, Sodinokibi_3b0c	14	1	2
BlackOut_ee13, Diavol_b3da, Diavol_7945, Diavol_2723, Play_006a, ViceSociety_HelloKitty_c249, RanzyLocker_0db6, Play_dd10	8	1	
Thanos_caf8, Thanos_8141, Thanos_66ed, Thanos_4852, Thanos_6e6b, Thanos_cbdb, Thanos_d29a	7	1	
MountLocker_00ed, MedusaLocker_f5fb, MedusaLocker_c2a0	3	1	
(BlackBasta_df5b, GlobeImposter_185f), (Rook_c2d4, LockBit_f2da)	2	2	
WannaCry_d103, Cuba_521c, Zeppelin_824a, Sugar_1d4f, DECAF_a471, Ransomare.Makop_a617, Stop_59d0, Conti_53b1, Intercobros_ade5, HelloXD_903c	1	10	
Hive_9e9f, Hive_0320, Hive_a45c, Nefilim_fb3f, Hive_460b, Hive_0302, Hive_dfa5, BianLian_eaf5, Hive_45fe, BianLian_46d3	10	1	3
(BlackMatter_8ead, BlackMatter_22d7, BlackMatter_e4fd, BlackMatter_c6e2, BlackMatter_730f, BlackMatter_b824, BlackMatter_2aad, BlackMatter_5da8), (LockBit_bdc2, LockBit_e216, LockBit_4bb1, LockBit_0545, LockBit_acad, LockBit_7340, LockBit_dd8f, LockBit_786a)	8	2	
(Maze_e8a0, Maze_3885, Maze_6a22), (GlobeImposter_e6fa, GlobeImposter_39f5, GlobeImposter_70fa)	3	2	
(RagnarLocker_10f9, RagnarLocker_5469), (BlackBasta_e281, BlackBasta_c4c8)	2	2	
RagnarLocker_afab, CryLock_4a47, RagnarLocker_041f, LIKEAHORSE_6d2e, DarkSide_f3f2, Rook_f87b, TimeTime_c535, Clop_bc1f, Maze_4e25	1	9	

D Hardware Specifications

Here we provide detailed calculations of the hardware requirements we presented in the main paper. First we calculate the number of multiplication required by each model for its forward pass. Other operations such as additions, exponentiation, etc. that are part of the forward pass as well, are much fewer and cheaper to implement in hardware and are therefore omitted here. We perform estimates for both the CLT and the PLT in the following section.

D.1 Calculations for the CLT

Following the model details found in Table 7, the CLT model architecture includes

- Embedding table of size $1024 \times 128 = 131072$
- Positional encoding of size $500 \times 128 = 64000$
- 3 self-attention encoder layers, each containing
 - W_Q, W_K, W_V matrices, each of size $128 \times 128 = 16384$ and total size of $3 \cdot 16384 = 49152$
 - Two fully connected layers, each of size $128 \times 128 = 16384$ and total size of $2 \cdot 16384 = 32768$
 - bias vectors, β, γ parameters for the layer norm, each of size 128 and total size of $4 \cdot 128 = 512$
- linear projection layer of size $128 + 1 = 129$
- 2×1 convolution kernel of size 2

The total number of parameters in the model is thus

$$131072 + 64000 + 3(49152 + 32768 + 512) + 129 + 2 \simeq 442K$$

The number of multiplications can similarly be derived for N - input vector of length 500

- For the self-attention we get
 - $NW_Q = Q, NW_K = K, NW_V = V$ is $500 \times 128^2 \simeq 8M$ each and $8M \cdot 3 \cdot 3 = 72M$ in total
 - $QK^T = X, XV$ is $500^2 \times 128 = 32M$ each and $32M \cdot 2 \cdot 3 = 192M$ in total
- For the fully connected layers we get
 - $500 \times 128^2 = 8M$ each and $8M \cdot 2 \cdot 3 = 48M$ in total
- For the final linear projection we get $500 \times 128 = 64K$

The total number of multiplications in a forward pass is thus

$$72M + 192M + 48M + 64K \simeq 312M$$

Finally, we note that since the CLT model works on by-command slices of 250 commands each, we may want to make sure it achieves the SSD throughput in random IOPS as well. The calculation is quite similar. For 312M multiplications per forward pass, a 300MHz hardware clock, 256 multipliers, and 250 commands per slice we get

$$\frac{250 \cdot 300\text{MHz} \cdot 256}{312M} \simeq 60K$$

IOPS Well above the spec of even the fastest SSD devices currently on the market.

subsectionCalculations for the PLT Following the model details found in Table 8, the PLT model architecture includes

- Embedding matrix of size $181 \times 512 = 92672$
- Positional encoding of size $100 \times 512 = 51200$

- 3 self-attention encoder layers, each containing
 - W_Q, W_K, W_V matrices, each of size $512 \times 512 = 262144$ and total size of $3 \cdot 262144 = 786432$.
 - Two fully connected layers, each of size $512 \times 2048 = 1048576$ and total size of $2 \cdot 1048576 = 2097152$.
 - bias vectors, β, γ parameters for the layer norm, each of size 512 and total size of $4 \cdot 512 = 2048$.
- linear projection layer of size $2 \times 512 + 2 = 1026$

The total number of parameters in the model is thus

$$92672 + 51200 + 6(786432 + 2097152 + 2048) + 1026 \simeq 17.5M$$

The number of multiplications can similarly be derived for N - input vector of length 100

- For the first embedding we get $181 \times 512 \times 100 = 9M$
- For the self-attention we get
 - $NW_Q = Q, NW_K = K, NW_V = V$ is $100 \times 512^2 \simeq 26.2M$ each and $26.2M \cdot 6 \cdot 3 = 472M$ in total
 - $QK^T = X, XV$ is $100^2 \times 512 = 5M$ each and $5M \cdot 2 \cdot 6 = 60M$ in total
- For the fully connected layers we get
 - $100 \times 512 \times 2048 = 105M$ each and $105M \cdot 2 \cdot 6 = 1258M$ in total
- For the final linear projection we get $100 \times 512 \times 2 = 102K$

The total number of multiplications in a forward pass is thus

$$9M + 472M + 60M + 1258M + 102K \simeq 1.8G$$